



# Molecular recognitive photocatalytic degradation of various cationic pollutants by the selective adsorption on visible light-driven $\text{SnNb}_2\text{O}_6$ nanosheet photocatalyst

Shijing Liang<sup>a</sup>, Ruowen Liang<sup>a</sup>, Linrui Wen<sup>a</sup>, Rusheng Yuan<sup>a</sup>, Ling Wu<sup>a,b,\*</sup>, Xianzhi Fu<sup>a</sup>

<sup>a</sup> Research Institute of Photocatalysis, Fujian Provincial Key Laboratory of Photocatalysis-State Key Laboratory Breeding Base, Fuzhou University, Fuzhou 350002, PR China

<sup>b</sup> State Key Laboratory of Structural Chemistry, Fujian Institute of Research on the Structure of Matter, Chinese Academy of Sciences, Fuzhou, Fujian 350002, PR China

## ARTICLE INFO

### Article history:

Received 22 February 2012

Received in revised form 14 May 2012

Accepted 20 May 2012

Available online 27 May 2012

### Keywords:

$\text{SnNb}_2\text{O}_6$

Nanosheet

Visible light

Selective adsorption

Selective photocatalysis

## ABSTRACT

Two-dimensional (2D) oxide nanosheet has attracted multidisciplinary study because of its unique physicochemical properties. In this work, a visible-light driven 2D nanosheet photocatalyst,  $\text{SnNb}_2\text{O}_6$  nanosheet (SNNS), has been applied into the selective photocatalysis for the first time. It is found that the SNNS sample exhibits significantly higher selectivity and superior activity for the photocatalytic degradation of positively charged pollutants from a mixture solution compared with the bulk  $\text{SnNb}_2\text{O}_6$ ,  $\text{TiO}_2$ , and N-doped  $\text{TiO}_2$  under visible light irradiation, even when the concentrations of other pollutants are much higher than those of cationic pollutants. This high selectivity and activity may be explained by the integrative effect of the unique crystal structure, highly selective adsorption performance, and oxidation of the photogenerated holes. By analyzing the results of X-ray photoelectron spectroscopy (XPS) and Fourier transform infrared (FT-IR) spectroscopy, as well as combining with the crystal structure of the nanosheet, the interaction between the SNNS sample and the pollutants has also been well investigated. In addition, the photocatalytic mechanism under visible light irradiation has also been discussed. Our current work may widen the application of the nanosheet and open promising prospects for the utilization of the nanosheet as visible light photocatalyst for selective degradation in environmental remediation.

© 2012 Elsevier B.V. All rights reserved.

## 1. Introduction

Over the past decades, semiconductor photocatalysis attracts much attention due to its universal applications especially in direct utilization of solar energy [1–4]. It is considered as a promising candidate to complement other advanced oxidation technologies in environmental remediation [5,6]. Recently, some researchers focus their efforts on the selective photocatalytic reactions [7–9]. This interest is due to the fact that it is difficult for the photocatalysis to remove all pollutants by itself [10]. Moreover, for the degradation of mixed organic pollutants, the high-level pollutants would be firstly degraded by a free-radical oxidation, while the target pollutants may be hardly removed [11]. In addition, achieving the selective degradation of targeted pollutants among the mixture may enhance the economical feasibility of the photocatalytic process for wastewater treatment [12].

To date, a series of selective photocatalytic reactions, which can be generally classified into two categories, have been reported. One is the selective transformation of organic functional groups [13], such as the hydroxylation of benzene and the selective oxidation of alcohols [14,15]. Unfortunately, the quantum efficiency, conversion ratio, and selectivity of these reactions are still low nowadays. The other is the selective photocatalytic degradation of organic compounds [16]. However, controlling the photocatalytic degradation of targeted pollutants via a selective route is a challenging issue since the reactivity of the free-radical is difficult to control. To achieve the molecular recognitive photocatalytic degradation efficiently, the followed conditions should be considered: (1) the photocatalysts show highly selective adsorption for targeted organic molecule; (2) the photocatalysts possess high surface area to accelerate the surface reaction. Currently, several approaches towards surface modification have been tried to increase the selective adsorption performance of the photocatalysts [17,18]. For example, Ghosh-Mukerji et al. reported that titanium dioxide mixed with  $\beta$ -cyclodextrin would efficiently enhance the selective photocatalytic degradation of benzene and 2-methyl-1,4-naphthoquinone in water [19]. Shen et al. developed a series of the molecular-imprinted organic polymers grafted titanium dioxide [20,21]. These photocatalysts exhibited high selective removal

\* Corresponding author at: Research Institute of Photocatalysis, Fujian Provincial Key Laboratory of Photocatalysis-State Key Laboratory Breeding Base, Fuzhou University, Fuzhou 350002, PR China. Tel.: +86 591 83779362; fax: +86 591 83779105.  
E-mail address: [wuling@fzu.edu.cn](mailto:wuling@fzu.edu.cn) (L. Wu).

of nitrophenols and chlorophenols under ultraviolet (UV) light irradiation. However, these organic–inorganic hybrid photocatalysts are quite instable since the organic component is also degraded through the photocatalytic oxidation [22]. Besides the photocatalysts' surface modification, the metal ions doped titanium dioxide [23–25], the coating of titanium dioxide particle with mesoporous silica and zeolite molecular sieve [26–29] as well as the use of titanasilicate molecular sieves [30–32], such as ETS-4, ETS-10 and TS-1, are other possible methods to solve the selective adsorption of reactants. Unfortunately, their photocatalytic activities are still low due to the recombination of the charge carriers accelerated over the dopants as well as the low content of titanium. In addition, most of these photocatalysts are the  $\text{TiO}_2$ -based photocatalysts which have a relatively wide bandgap and are only active under UV light. In view of the efficient utilization of solar energy, the development of single-phase photocatalysts with a high performance to selectively degrade targeted molecular species under visible light irradiation is of great significance.

Layered compounds built by a series of charged sheets are one of the most attractive functional materials because their large inner surface areas are potential application in the various catalytic reactions [33]. For example, layered titanates have been developed to selectively decompose benzene from an aqueous mixture of benzene, phenol, and 4-butylphenol under UV light irradiation [34]. However, the high charge density of the sheets makes it difficult for reactant molecules to associate with the layered sheets [35]. Exfoliation of the layered sheets, forming the two-dimensional (2D) oxide nanosheets, may be an alternative way to overcome this disadvantage. Furthermore, the photocatalysts with different surface charges would exhibit a highly selective adsorption of charged targeted pollutants and a molecular recognitive photocatalytic performance via the electrostatic attraction or repulsion [36,37]. Therefore, these 2D nanosheet photocatalysts with high charge density may be considered to be efficiently applied into selective degradation of charged pollutants.

In this work, we report for the first time that the visible-light driven 2D nanosheet photocatalysts exhibit an adsorption-driven molecular recognitive photocatalytic reaction.  $\text{SnNb}_2\text{O}_6$  nanosheet (SNNS) photocatalyst prepared by hydrothermal reaction without exfoliation has been taken as a typical example. In photocatalytic process, the SNNS sample shows significantly high selectivity and activity for the degradation of cationic dyes from the mixture solution under visible light irradiation. The nature of this high selectivity and activity would be explained by the crystal structure, adsorption performance, and active species. Meanwhile, the adsorption modes of dyes and a possible photocatalytic mechanism over the nanosheet have also been discussed and proposed. It is hoped that our work could provide a new insight into the selective photocatalysis applied in the wastewater treatment.

## 2. Experimental

### 2.1. Preparation of catalysts

The  $\text{SnNb}_2\text{O}_6$  (SN) was prepared by a facile hydrothermal (HT) reaction using  $\text{Nb}_2\text{O}_5 \cdot n\text{H}_2\text{O}$  as a precursor which was obtained from a simple procedure we reported previously [38]. Briefly, the mixture of the as-obtained  $\text{Nb}_2\text{O}_5 \cdot n\text{H}_2\text{O}$  and  $\text{SnCl}_2$  in a molar ratio of  $\text{Nb}^{5+}:\text{Sn}^{2+} = 2:1$  was dispersed into 70 mL deionized water, and then was transferred to a 100 mL Teflon-lined stainless steel autoclave. After that, the pH values were adjusted by  $4 \text{ mol L}^{-1}$  NaOH under vigorous stirring. A nitrogen gas of  $30 \text{ mL min}^{-1}$  was purged for 2 h to exclude oxygen gas prior to heating. The autoclave was sealed and heated in an oven at  $200^\circ\text{C}$  for 48 h under autogenous pressure. After cooled naturally, the products were centrifuged, washed with

deionized water and dried at  $60^\circ\text{C}$  in an oven. The samples were denoted SN- $n$  ( $n$  is pH value), for example, sample SN-2 meant that the sample prepared under pH 2. As a comparison, bulk  $\text{SnNb}_2\text{O}_6$  (defined as SN-SSR) was prepared by a traditional solid reaction using  $\text{Sn}_3(\text{OH})_2\text{O}_2$  as a precursor based on earlier work [39,40]. N-doped  $\text{TiO}_2$  was prepared following our previous work [41].

### 2.2. Characterization

The as-prepared samples were characterized by powder X-ray diffraction (XRD) on a Bruker D8 Advance X-ray diffractometer operated at 40 kV and 40 mA with Ni-filtered  $\text{Cu K}\alpha$  irradiation ( $\lambda = 1.5406 \text{ \AA}$ ). The Brunauer–Emmett–Teller (BET) surface area was measured with an ASAP2020M apparatus (Micromeritics Instrument Corp.). UV–vis diffuse reflectance spectra (UV–vis DRS) were obtained by using a UV–vis spectrophotometer (Varian Cary 500) and the data were converted to Kubelka–Munk (KM) functions. Barium sulfate was used as a reference. Transmission electron microscopy (TEM) images were recorded using a JEOL model JEM 2010 EX microscope at an accelerating voltage of 200 kV. A tapping-mode atomic force microscopy (AFM, Nanoscope Multimode IIIa, Veeco Instruments) with Si-tip cantilever was used to evaluate the morphology of the obtained nanosheets on the mica substrate. X-ray photoelectron spectroscopy (XPS) measurements were performed on a PHI Quantum 2000 XPS system with a monochromatic Al  $\text{K}\alpha$  source and a charge neutralizer. For XPS experiments detecting the changes of the N 1s binding energy, dyes were first adsorbed on sample SN-2 followed by centrifugation and separation, and then the solid catalysts were washed completely to remove the physically adsorbed dyes molecules. The washed samples were dried under vacuum at  $100^\circ\text{C}$ . The above process was carried out in the dark to ensure that no photoreaction would occur during the sample treatment. The infrared spectra of dyes adsorbed on the catalysts were obtained on a Nicolet Nexus 670 Fourier transform infrared (FT-IR) spectrometer at a resolution of  $4 \text{ cm}^{-1}$ . A total of 64 scans were performed to obtain each spectrum. The samples used in this experiment were prepared by the same process as that in the XPS measurements. The electrophoretic mobility of SN-2 particles in aqueous suspensions ( $0.1 \text{ g/L}$ ) was measured to determine its  $\zeta$ -potential as a function of pH using a Zetasizer 3000 instrument (Malvern Co., UK) at  $25^\circ\text{C}$ . Electron spin resonance (ESR) signals of spin-trapped paramagnetic species with 5,5-dimethyl-1-pyrroline N-oxide (DMPO) were recorded with a Bruker A300 spectrometer. A 300 W Xe lamp (Beijing Trustech, PLS-SXE300c) with a 420 nm cut-off filter was used as a light source.

### 2.3. Electrochemistry measurement

The working electrode was prepared on indium-tin oxide (ITO) glasses, which was cleaned by sonication in chloroform, acetone and ethanol for 30 min, respectively. The glass was then rinsed with millipore water and kept in isopropanol for 24 h. 50 mg powder was mixed with 2 mL dimethylformamide under sonication for 30 min to get slurry. The slurry was spreading onto ITO glass whose side part was previously protected using Scotch tape. A copper wire was connected to the side part of the ITO glass using a conductive tape. Uncoated parts of the electrode were isolated with epoxy resin, and the exposed area of the electrode was  $0.25 \text{ cm}^2$ . Electrochemical measurements were performed in a conventional three electrode cell, using a Pt plate and a saturated Ag/AgCl electrode as counter electrode and reference electrode, respectively. The working electrodes were immersed in a  $0.2 \text{ M Na}_2\text{SO}_4$  aqueous solution (pH 6.6) without additive for 30 s before measurement was carried out. For Mott–Schottky experiments, the potential ranged from  $-0.5$  to

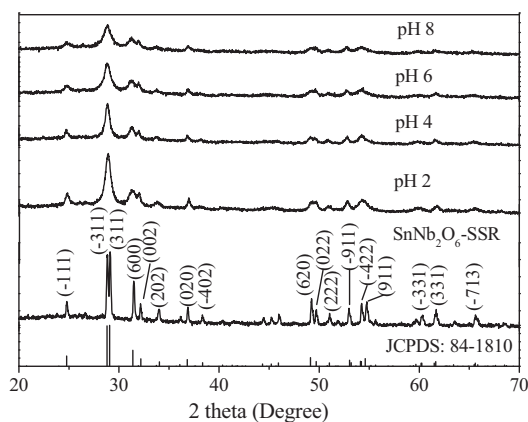


Fig. 1. XRD patterns of SN-SSR and  $\text{SnNb}_2\text{O}_6$  prepared under different pH values.

0.5 V (vs. Ag/AgCl), and the perturbation signal were 20 mV with the frequency from 1.5 to 0.5 kHz.

#### 2.4. Adsorption performances of $\text{SnNb}_2\text{O}_6$

Adsorption studies of various dyes on  $\text{SnNb}_2\text{O}_6$  were carried out in a 100 mL Pyrex glass vessel which contained 80 mL dyes solution (10 ppm) under dark condition. After adding the catalyst with a certain amount, the sample was sampled per 2 min under vigorous stirring. And then, the suspension was rapidly centrifuged to solid–liquid separation. The dyes concentration was quantified by UV–vis spectroscopy (Varian Cary 50).

#### 2.5. Evaluation of photocatalytic activity

The photocatalytic activities of  $\text{SnNb}_2\text{O}_6$  were evaluated by the decomposition of dyes in an aqueous solution. The catalyst (20 mg) was suspended in a 100 mL Pyrex glass vessel which contained 80 mL dye solutions. The light source was a 500 W halogen lamp (Philips Electronics,  $20 \text{ mW cm}^{-2}$  at 420 nm) and two cut-off filters were used to occlude light below 420 nm and above 760 nm to ensure the photoreaction proceeded under visible-light irradiation. The suspensions were stirred in the dark for 120 min to ensure adsorption–desorption equilibrium prior to irradiation. During irradiation, 2 mL of the suspension was removed at given time intervals for subsequent dyes concentration analysis following centrifugation. The dyes concentration was analyzed by an UV–vis spectrophotometer (Varian Cary 50). The mineralization ratio of dyes solution was determined by total organic carbon (TOC) value which obtained by a TOC analyzer (TOC-VCPH, Shimadzu, Japan).

### 3. Results and discussion

#### 3.1. Crystal structure and surface area

Fig. 1 shows the XRD patterns of the as-prepared products obtained by HT reaction. It is clear that the diffraction peaks can be exactly indexed to the pure phase of  $\text{SnNb}_2\text{O}_6$  (JCPDS: 84-1810; Monoclinic phase; Space group:  $\text{C2/c}$ ). No impurity peaks such as those of  $\text{SnO}$ ,  $\text{SnO}_2$  or  $\text{Nb}_2\text{O}_5$  are detected. The crystallinities of the samples are decreased with increasing the pH values. This may be ascribed to their different Sn precursors [42] and reaction rates. Interestingly, the intensity of the diffraction peak at  $2\theta = 31.4^\circ$  (corresponding to (600) lattice plane) from the SN-2 sample is much lower than that of the same diffraction peak from the SN-SSR sample. This is implied that the thickness of the SN-2 sample is greatly decreased compared with that of the SN-SSR sample in the x axis direction. The BET surface areas for the SN-*n* samples

prepared at different pH values are almost the same (ca.  $44 \text{ m}^2/\text{g}$ ). They are much higher than that of SN-SSR sample ( $1.3 \text{ m}^2/\text{g}$ ). The adsorption–desorption isotherms of the SN-*n* samples belong to type II isotherm (see Fig. S1, Supporting Information), which suggested that the morphologies of the SN-*n* samples would be sheet.

#### 3.2. Morphology analysis

The morphologies of the products have been characterized by TEM. Fig. 2 shows that sample SN-2 is composed of numerous nanosheets (NSs) with a thickness of 1–4 nm versus several hundred nanometres in lateral size. The surfaces of these nanosheets are much glazed, agreeing well with the results of  $\text{N}_2$ -sorption (Fig. S1). AFM image (Fig. S2) further confirms that the morphology of the SN-2 sample is 2D nanosheet and the thickness of the monolayer nanosheet is about 0.8 nm. Considering that the  $\text{SnNb}_2\text{O}_6$  is a typical layered niobate built by polyanion layer with a thickness of 0.85 nm (Fig. S3), these SN-2 nanosheets consist of polyanion layer of 1–5. Due to the high charge density of the sheets on layered catalyst, the intercalation of reactant molecules associated with the active sites on catalyst's inner surface is difficult. This nanosheet morphology can efficiently overcome this disadvantage on the bulk counterpart, enhancing the photocatalytic activity. As shown in Fig. 2c, clear lattice fringes can be observed. The fringes of  $d = 0.36 \text{ nm}$  match those of the  $(-1\ 1\ 1)$  lattice plane of monoclinic  $\text{SnNb}_2\text{O}_6$ . A typical selected area electron diffraction (SAED) pattern of  $\text{SnNb}_2\text{O}_6$  nanosheet (SNNS) reveals that the sample has single-crystalline character (Fig. 2d). For sample SN-6, although the nanosheet morphology is maintained, an increased thickness and irregular morphology have been observed (Fig. S4a). It may be ascribed to that the precursor transforms from  $\text{Sn}(\text{OH})\text{Cl}$  to  $\text{Sn}_3(\text{OH})_2\text{O}_2$  after increasing the pH value, resulting in the decreased reaction rate. The HRTEM image and typical SAED pattern reveal that sample SN-6 still exhibits high crystallinity and single-crystalline character (Fig. S4b).

#### 3.3. Photoabsorption performance

As the photoabsorption property plays a key role in determining the photocatalytic activity, the UV–vis diffuse reflectance spectra of the samples were measured. Obviously, the samples have a strong absorption in the visible light region (Fig. 3). The absorption bands of the samples with the steep edges indicate a transition from the valence band to the conduction band [43], further confirming that the samples are pure SN sample. The band gaps of the samples are estimated about 2.6 eV, while that of the SN-SSR sample is 2.3 eV. This may be ascribed to the quantum size effect. Moreover, the result indicates that the photogenerated charge carriers on the SN-*n* samples would exhibit the higher redox ability compared that of the SN-SSR sample.

#### 3.4. Photocatalytic properties

The photocatalytic activity of the SNNS sample is firstly evaluated via the degradation of zwitterionic dye, rhodamine B (RhB), under visible light irradiation. Fig. 4 shows that the photolysis of RhB can be negligible. Moreover, the concentration of RhB does not change in the presence of the catalysts under dark condition. Therefore, the presence of both visible light and photocatalyst is necessary for the photocatalytic reaction to proceed. Under visible light irradiation, all the catalysts show the obvious photocatalytic activities for degradation of RhB. Because the conduction band level of  $\text{SnNb}_2\text{O}_6$  (ca.  $-1.0 \text{ V}$  vs. NHE, normal hydrogen electrode, Fig. S5) is very close to the  $E^0(\text{RhB}^*/\text{RhB}^+)$  ( $-1.09 \text{ V}$ ) [44], the degradation rate of dye by the photosensitization is very slow under visible light irradiation. Moreover, the photocurrent experiment confirms



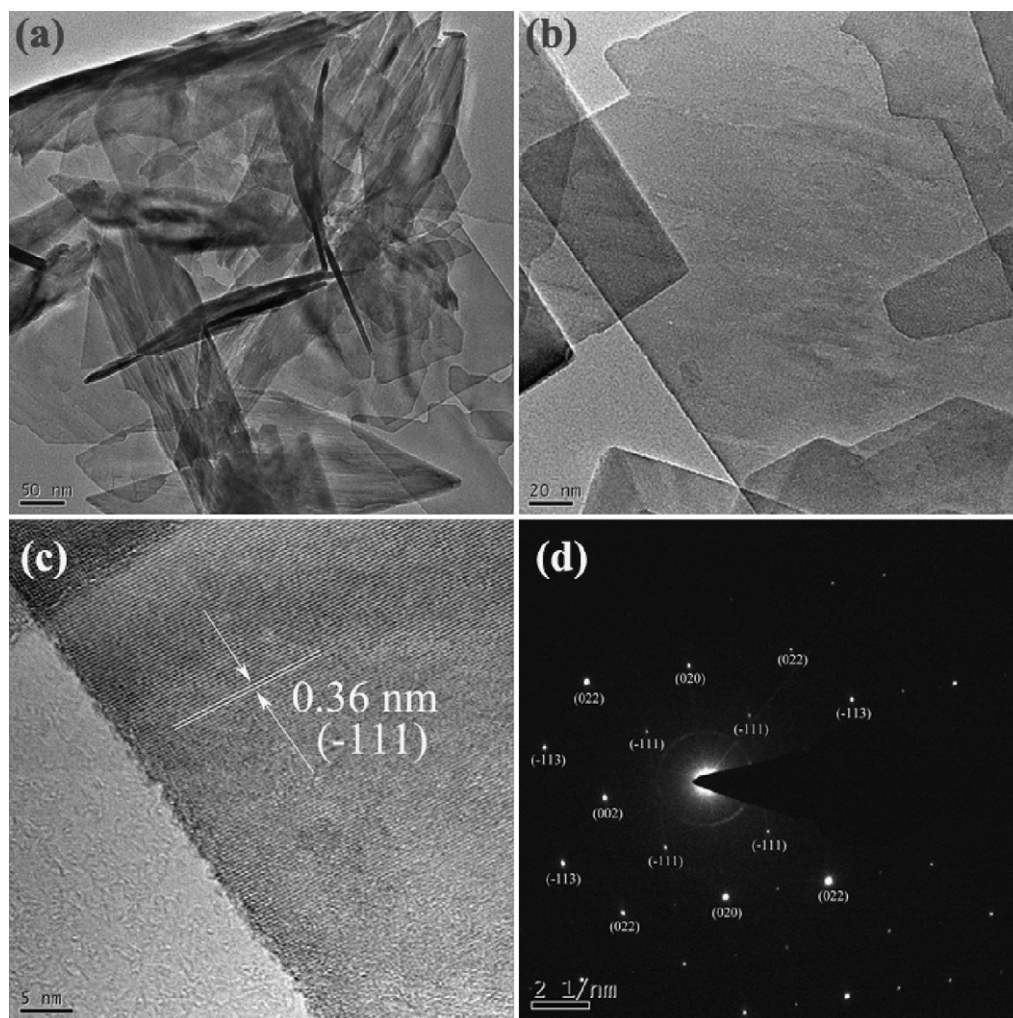


Fig. 2. TEM, HRTEM images and typical SAED pattern of sample SN-2.

that the photogenerated electron–hole pairs of  $\text{SnNb}_2\text{O}_6$  can be efficiently separated under visible light irradiation (Fig. S6). In other words, the degradation of RhB over  $\text{SnNb}_2\text{O}_6$  may be directly brought about by photogenerated oxidants via the typical photocatalytic reaction routes. The photocatalytic activities of the SN-*n* samples strongly depend on the synthetic pH values. A reduction

in the efficiency is observed with the increase of the pH value. The sample prepared under pH 2 exhibits the highest activity. Total organic carbon (TOC) analysis demonstrates that about 20% RhB has been destroyed into  $\text{CO}_2$  and  $\text{H}_2\text{O}$  over the SN-2 sample after visible light irradiation for 6 h. The degradation of RhB is found

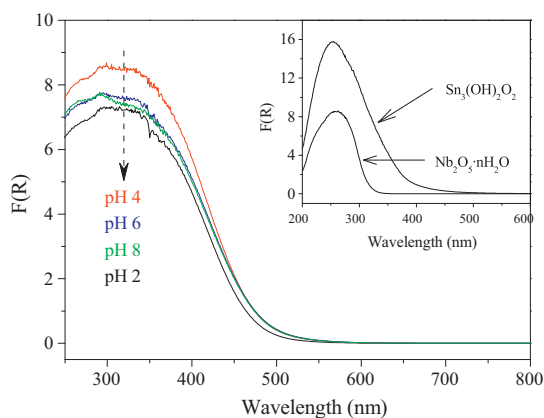


Fig. 3. UV-vis DRS of  $\text{SnNb}_2\text{O}_6$  and the precursors (inset).

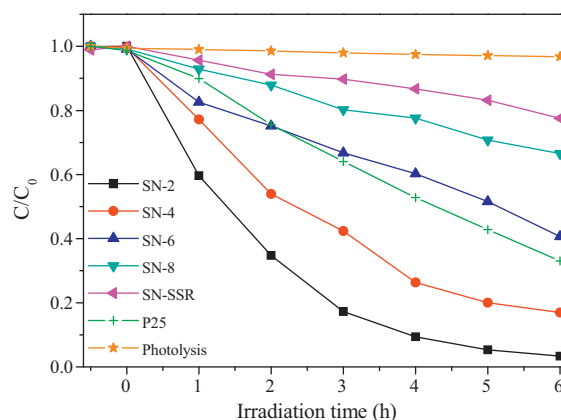
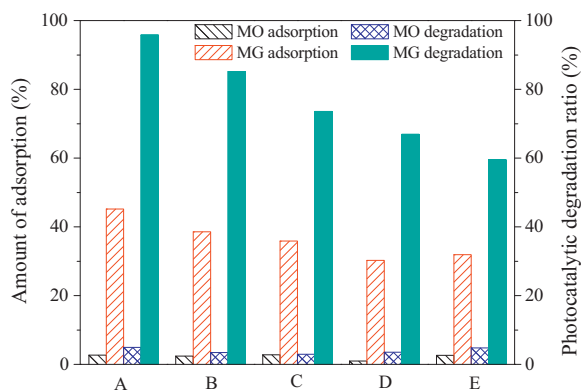


Fig. 4. Temporal concentration changes of the RhB solution over the samples prepared by different conditions under visible light irradiation.



**Fig. 5.** Adsorption and photocatalytic performances of  $\text{SnNb}_2\text{O}_6$  nanosheet toward mixture dyes (under visible light irradiation for 5 h): A: 10 ppm MG + 5 ppm MO; B: 10 ppm MG + 10 ppm MO; C: 10 ppm MG + 20 ppm MO; D: 10 ppm MG + 30 ppm MO; E: 10 ppm MG + 40 ppm MO.

to follow the pseudo-first-order decay kinetics (Fig. S7). The photodegradation constant of the SN-2 sample reaches  $0.58 \text{ h}^{-1}$ , which is over 14 and 3 times higher than those of the SN-SSR sample ( $0.04 \text{ h}^{-1}$ ) and  $\text{TiO}_2$  ( $0.17 \text{ h}^{-1}$ ), respectively. The high visible-light photocatalytic activities of the SN-2 sample could be attributed to the high surface area, strongly absorbing visible light, and the unique nanosheet structure. Fig. S8 shows a hypsochromic shift of the absorption maximum during the photocatalytic process plotted versus the reaction time. Obviously, the maximum absorbance of RhB exhibited a marked blue shift. This hypsochromic shift has been proven to be derived from the formation of N-de-ethylated intermediates in the photocatalytic degradation of RhB [45,46]. The result suggests that RhB is adsorbed on the catalyst's surface via the positively charged  $-\text{N}(\text{Et})_2$  group. In addition, the possibility of selective photocatalysis over the SNNS samples is suggested.

To confirm the SNNS samples with high selective photocatalytic activity, the photocatalytic degradations of the mixture dyes (methyl orange (MO) and malachite green (MG)) with different concentrations have been carried out. As shown in Fig. 5, the SNNS sample exhibits high adsorption ability for MG in all experimental conditions although the adsorption amount is slightly decreased with increasing the other dye's concentration. However, for anionic MO, the photocatalyst almost does not adsorb it, even when its concentration has been greatly increased. These results reveal that the SNNS sample can recognize the targeted pollutants from the aqueous mixture efficiently regardless of whether with or without higher concentration than the other pollutants. Under visible light irradiation, the targeted pollutant, cationic MG, is rapidly degraded over SNNS sample, while the photocatalytic activity of SNNS sample for decomposing MO is very low. In the mixture with 10 ppm MG and 5 ppm MO, the photocatalytic degradation ratio of MG reaches 96%, whereas only about 4% MO has been degraded under visible light irradiation for 5 h. With increasing the MO concentration in the mixture, the photocatalytic degradation ratio of MG has been gradually decreased. It may be attributed to the fact that the transmission of MG from the bulk solution to the photocatalyst's surface has been prevented by MO molecules. Interestingly, when the MO concentration is 40 ppm in the mixture, which is much higher than that of MG, the degradation ratio of MO is still very low. As a comparison, the adsorption and photocatalytic performances of SN-SSR,  $\text{TiO}_2$  (Degussa P25), and N-doped  $\text{TiO}_2$  toward mixture dyes have also been evaluated under the same conditions (Fig. S9). It is surprised that the selectivities and activities of these photocatalysts are very low. These results indicate that the SNNS sample exhibits a selectively photocatalytic degradation of cationic dye from an

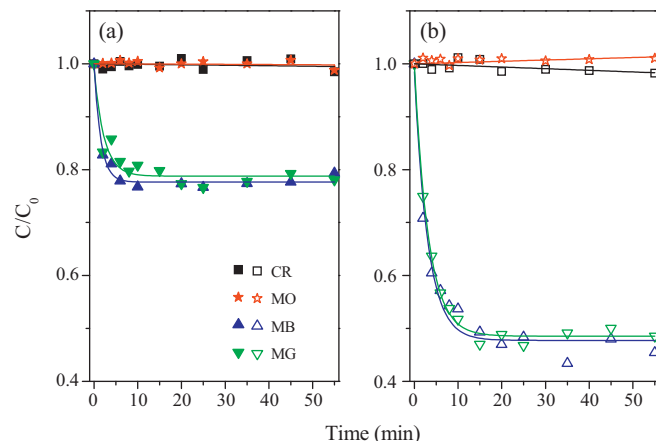


**Fig. 6.** Temporal concentration changes of the dye solutions over the SN-2 sample without light irradiation: (a) 10 mg catalyst; (b) 20 mg catalyst.

aqueous mixture and would be a promising photocatalyst used into wastewater treatment.

### 3.5. Selective adsorptions of dyes

Why the SNNS sample could show the high selectivity in the photocatalytic degradation? What are the main influence factors? Generally, in a selective photocatalytic reaction process, the selectivity is resulted from a synergistic effect of several key factors, such as the adsorption property of the targeted reactant, the morphology of the photocatalyst, and the active species. Considering that the nanosheet morphology cannot be used in the selective photocatalysis by sharp- and size-control and the SNNS sample exhibits a high selective adsorption for MG from the mixture solution, the high selective photocatalytic degradation may be ascribed to the adsorption property and the active species. In order to further distinguish the selective adsorption performance of sample SNNS, a series of dyes with different charges (such as: congo red (CR), MO, methylene blue (MB), and MG (Fig. S10)) have been chosen as targeted pollutant. The results are shown in Fig. 6. Obviously, the cationic substrates such as MB and MG are strongly adsorbed on sample SNNS, while the anionic substrates such as CR and MO are hardly adsorbed on the photocatalyst. Even when the amount of the sample is increased, the anionic dyes are almost no adsorbed yet. This result is consistent with color evolution of sample SN with or without adsorbing dyes (Fig. S11). In addition, the adsorption-desorption equilibrium of the cationic dyes can be quickly arrived after 20 min without light irradiation. These implied that the decreased concentrations of the dyes are caused by the adsorption instead of reaction. The highly selective adsorption for the dyes may be reasonably explained as the electrostatic attraction or repulsion between the negatively charged  $\text{SnNb}_2\text{O}_6$  framework (SNFW) and the charged dyes. For the SNFW, it is consisted of a series of two-octahedron-thick sheet (polyanion layer) and the  $\text{Sn}^{2+}$  ions inserted between two sheets (Fig. S2). The polyanion layer built by edge-sharing octahedral  $\text{NbO}_6$  units exhibits a negative charge. Simultaneously, the morphology of nanosheet would enhance the external surface charge of the sample. Therefore, the product shows a high adsorption capacity for the cationic dyes, while it does not adsorb the anionic dye molecules. This conclusion can be reconfirmed from the result of zeta potential measurement. Fig. S12 shows that the point of zero zeta potential (PZZP) of sample SN-2 is at ca. pH 2.5. As a result, the surface of sample SN-2 is dominated by negative charges at neutral solution (the actual reaction condition in our system).

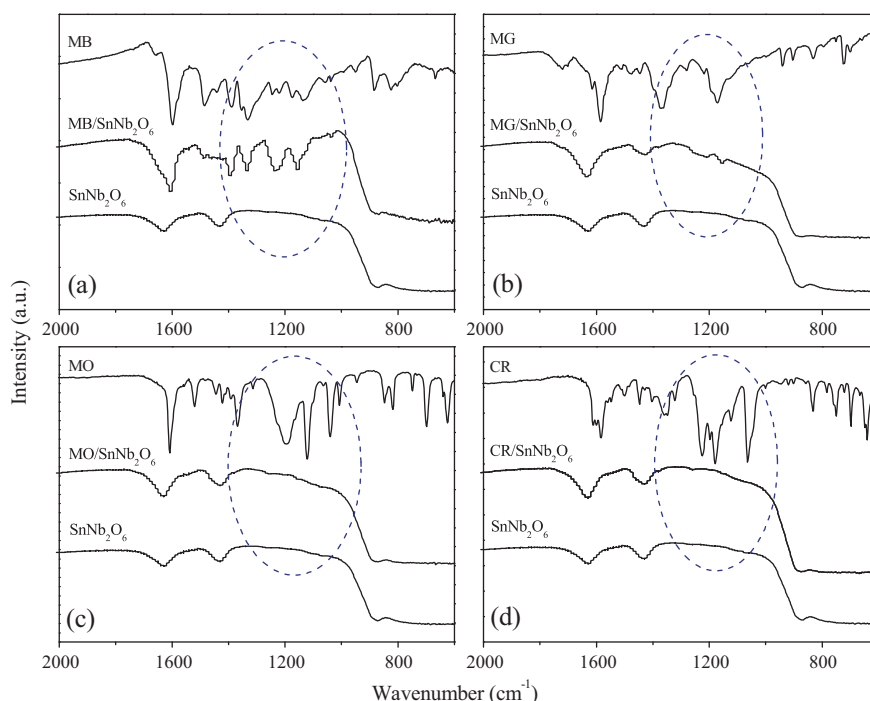


Fig. 7. FT-IR spectra of sample SN-2 and dyes adsorbed SN samples: (a) MB; (b) MG; (c) MO; (d) CR.

### 3.6. FTIR analysis

The interaction between the SN sample and the dyes has been further investigated by the FT-IR and XPS. Fig. 7 shows the FT-IR spectra of sample SN-2 before and after adsorbing dyes. Compared with the fresh SN-2 sample, MB/SN sample displays that some new strong vibration bands appear in the region of  $1000\text{--}1400\text{ cm}^{-1}$ . The bands at  $1387$  and  $1325\text{ cm}^{-1}$  are assigned to the symmetric stretch of C-N and the symmetric deformation of  $-\text{CH}_3$ , respectively [47]. Interestingly, these bands on the pure MB are at  $1398$  and  $1354\text{ cm}^{-1}$  (Fig. 7a) [48]. The band shifted to smaller wavenumber which indicates the interaction between sample SN-2 and the dimethylamine group on MB. Meanwhile, the other vibration bands are also observed in  $2800\text{--}3000\text{ cm}^{-1}$  region (Fig. S13a), which are contributed by the vibrations of the carbon-hydrogen bond [47]. For MG/SN sample, the similar phenomenon could be clearly observed (Fig. 7b and Fig. S13b). In contrast, only some vibrations of the carbon-hydrogen bond have been observed on the anionic dyes adsorbed sample SN-2 in the region of  $2800\text{--}3000\text{ cm}^{-1}$  (Fig. S13c and d). It may be explained that some anionic dyes are physically adsorbed on the surface of the sample SN-2 despite most of anionic dyes have been removed by water washing. In the low wavenumber region, there is no obviously new band and the vibrations at  $1400\text{--}1700\text{ cm}^{-1}$  remain nearly unchanged (Fig. 7c and d). These facts suggest that the cationic dyes adsorb on the surface of the sample SN through the physical and chemical processes, while the anionic dyes are only adsorbed by physical process.

### 3.7. XPS analysis

Fig. 8 shows the N 1s XPS spectra of pure MB as well as MB and MO adsorbed on sample SN-2. The XPS peak of N 1s in pure solid MB dye is located at  $399.1\text{ eV}$  (Fig. 8a). Observation of the N 1s spectrum for MB adsorbed SN-2 sample (Fig. 8b), the curve could be deconvoluted into two peaks, located at  $401.0$  and  $399.1\text{ eV}$ , respectively. The N 1s with higher binding energy (BE) may be attributed to the specific interaction of the  $-\text{N}(\text{Me})_2$  group with the sample SN-2 surface. For MO adsorbed SN-2 sample, no signal for N 1s is

observed (Fig. 8c). It indicates the MO has not interaction with sample SN-2. These results suggest again the above conclusion obtained from the FT-IR results. Moreover, because the MB adsorbed sample SN-2 for XPS measurement has been washed thoroughly by water, the MB adsorbed by physical process would be almost removed. The MB adsorbed on sample SN-2 may be only derived from chemical adsorption process. Therefore, we may conclude that MB stands on the surface of the catalyst through one dimethylamine group from the following considerations: (1) The N 1s peaks in the XPS spectrum revealed that there are two kinds of N species on the photocatalyst's surface. It is reasonable to ascribe one to direct-adsorbed  $-\text{N}(\text{Me})_2$  and the other primarily to the untouched  $-\text{N}(\text{Me})_2$ . They are in the identical MB molecule because the ratio of two peak areas is nearly 1:1. (2) It is known that the positive charge on MB is resonant between the two dimethylamine groups of the MB chromophore. Once one of the dimethylamine groups adsorbs on the catalyst's surface, the resonance should be destroyed, which causes the positive charge to center at the adsorbed dimethylamine and favors the mode of single-dimethylamine adsorption.

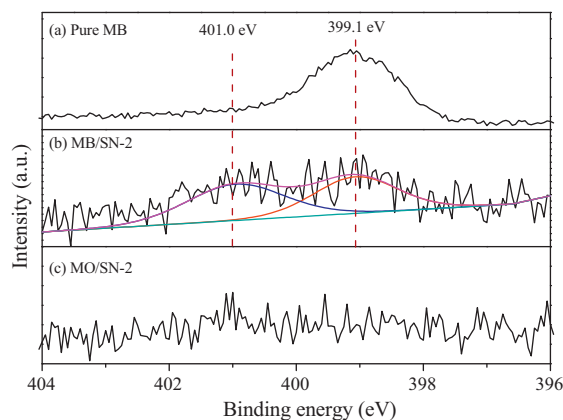
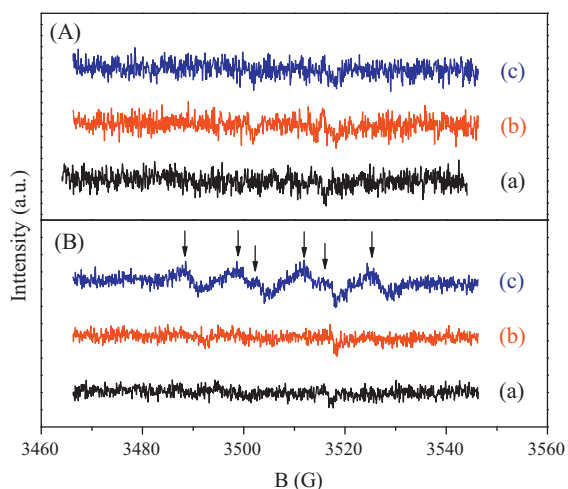


Fig. 8. N 1s XPS spectra of pure MB (a) as well as MB (b) and MO (c) adsorbed on sample SN-2.





**Fig. 9.** DMPO spin-trapping ESR spectra in samples aqueous dispersion for (A) DMPO-•OH and (B) DMPO-•O<sub>2</sub><sup>-</sup>: (a) without the nanosheet, irradiated for 300 s; (b) with the nanosheet, without light; (c) with the nanosheet, irradiated for 300 s.

### 3.8. Roles of the active species

Besides the adsorption performance of the SNNS sample, the active species in the reaction process are also a key factor that affects the photocatalytic reaction. Considering the photocatalytic reaction dominated by the free-radical mechanism, the selectivity would be low. We infer that the main active species in the selective photocatalysis may be the photogenerated holes. To learn the involvement of active radical species in the photocatalytic process, the electron spin resonance (ESR) spin-trap technique (with 5,5-dimethyl-1-pyrroline N-oxide (DMPO)) was firstly employed to probe the reactive oxygen species generated during visible light irradiation. As shown in Fig. 9, no peaks of DMPO-•OH are obviously observed under visible light irradiation, while sextet characteristic peaks of DMPO-•O<sub>2</sub><sup>-</sup> adduct are observed in methanol dispersion. Furthermore, no signals can be detected without irradiation or catalyst. These results reveal that the •O<sub>2</sub><sup>-</sup> radicals can be produced over the nanosheet under visible light irradiation. No •OH radicals can be well explained by the relatively low potential energy of the valence band (VB) holes ( $E_{VB}^0 = 1.6 \text{ eV}$ , Fig. S6).

What is the role of the •O<sub>2</sub><sup>-</sup> radicals during the photocatalytic process? Does it play a key role in the photodegradation reaction? To further investigate the photogenerated holes and •O<sub>2</sub><sup>-</sup> radicals, a series of the control experiments, such as adding scavenger for holes and electrons into the photocatalytic process, were carried out. As shown in Fig. 10, with 0.1 g of ammonium oxalate (AO) as a hole-scavenger added to the solution [49], the rate for degradation of MG over the nanosheet is remarkably decreased. This suggests that the holes play a very important role toward the degradation of MG under visible light irradiation. Meanwhile, this low photocatalytic activity also demonstrates that the photosensitization effect of MG may be negligible. In the saturated N<sub>2</sub> system, the photocatalytic activity is decreased. However, the photodegradation inhibition effect is obviously less than that on AO. Since the VB holes of the nanosheet cannot oxidize the adsorbed hydroxyl species into •OH, the VB holes are mainly responsible for the oxidation of MG over the nanosheet, while the active species generated by electrons, such as •O<sub>2</sub><sup>-</sup> radicals, play a minor role in the photodegradation of MG in this work. Although the photocatalytic activity has been increased in the bubbling O<sub>2</sub> (Fig. 10), dissolved O<sub>2</sub> mainly services as an efficient electron scavenger to accelerate the separation of photogenerated electron-hole pairs. In other word, the enhancement of the photocatalytic performance is ascribed to the increased concentration of photogenerated holes in the presence of O<sub>2</sub>. The

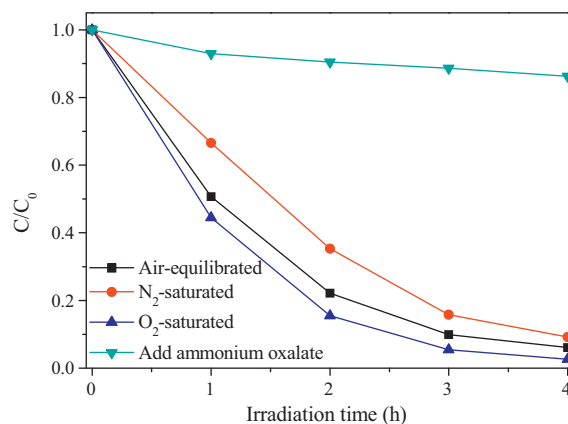


**Fig. 10.** Photocatalytic degradation of MG over the SNNS sample under different conditions irradiated by visible light irradiation.

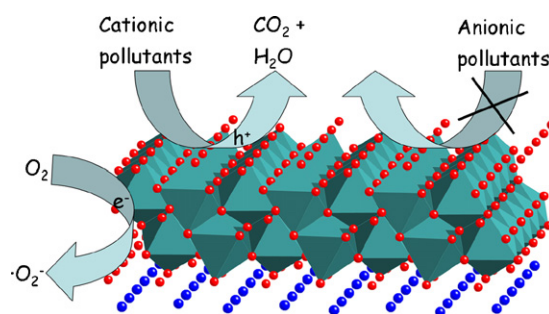


**Fig. 11.** Scheme diagram of the selective photocatalytic reaction.

similar phenomenon has also been observed in the degradation of RhB (Fig. S14). It could well explain the deethylation of RhB in the photocatalytic process.

### 3.9. Possible photocatalytic mechanism

Base on the experimental results, a possible mechanism for selectively degraded organic pollutant over the nanosheet was proposed, and was illustrated in Fig. 11. The targeted reactants are selectively adsorbed on the nanosheet via the electrostatic attraction from the mixture solution. Under visible light irradiation, a charge carrier has been produced and the photogenerated hole is transferred to the catalyst's surface quickly. Subsequently, the photocatalytic degradation would start from holes attacking. At the same time, the photogenerated electron is excited from the valence band of SnNb<sub>2</sub>O<sub>6</sub> to its conduction band (CB). And then the adsorbed O<sub>2</sub> captures this photogenerated electron to accelerate the separation of photogenerated electron-hole pairs. In addition, for our photocatalyst, the photogenerated electrons can reduce the oxidation of the Sn<sup>2+</sup> ions to keep the stability of photocatalyst.

## 4. Conclusion

In summary, a visible-light driven 2D nanosheet photocatalyst, SnNb<sub>2</sub>O<sub>6</sub> nanosheet (SNNS) prepared by hydrothermal reaction without exfoliation, has been applied into the selective photocatalysis for the first time. We have demonstrated that the SNNS sample exhibits significantly higher selectivity and superior activity for the photocatalytic degradation of positively charged pollutants from a mixture solution compared with the bulk SnNb<sub>2</sub>O<sub>6</sub>, TiO<sub>2</sub>, and N-doped TiO<sub>2</sub> under visible light irradiation, even in the presence of other high-level pollutants. This high selectivity and activity may be explained by the integrative effect of the unique crystal

structure, high selective adsorption performance, and oxidation of the photogenerated holes.

## Acknowledgments

The work was supported by the National Natural Science Foundation of China (21177024), Natural Science Foundation of Fujian Province (2010J01035 and 2011J01041), Basic Research Program of China (973 Program: 2011CB612314) and Program for Changjiang Scholars and Innovative Research Team in University (PCSIRT0818).

## Appendix A. Supplementary data

Supplementary data associated with this article can be found, in the online version, at <http://dx.doi.org/10.1016/j.apcatb.2012.05.017>.

## References

- [1] Y. Horiuchi, H. Yamashita, *Applied Catalysis A: General* 400 (2011) 1–8.
- [2] D. Zhang, G. Li, J.C. Yu, *Journal of Materials Chemistry* 20 (2010) 4529–4536.
- [3] C. Chen, W. Ma, J. Zhao, *Chemical Society Reviews* 39 (2010) 4206–4219.
- [4] M.R. Hoffmann, S.T. Martin, W. Choi, D.W. Bahnemann, *Chemical Reviews* 95 (1995) 69–96.
- [5] A. Kubacka, M. Fernández-García, G. Colón, *Chemical Reviews* 112 (2012) 1555–1614.
- [6] S. Liang, L. Shen, J. Zhu, Y. Zhang, X. Wang, Z. Li, L. Wu, X. Fu, *RSC Advances* 1 (2011) 458–467.
- [7] T. Ohno, T. Tsubota, K. Kakiuchi, S. Miyayama, K. Sayama, *Journal of Molecular Catalysis A: Chemical* 245 (2006) 47–54.
- [8] P. Roy, T. Dey, K. Lee, D. Kim, B. Fabry, P. Schmuki, *Journal of the American Chemical Society* 132 (2010) 7893–7895.
- [9] H. Park, W. Choi, *Journal of Physical Chemistry B* 109 (2005) 11667–11674.
- [10] G. Li, S. Park, D.-W. Kang, R. Krajmalnik-Brown, B.E. Rittmann, *Environmental Science and Technology* 45 (2011) 8359–8367.
- [11] K. Inumaru, T. Kasahara, M. Yasui, S. Yamanaka, *Chemical Communications* (2005) 2131–2133.
- [12] Y. Wang, W. Ma, C. Chen, X. Hu, J. Zhao, J.C. Yu, *Applied Catalysis B* 75 (2007) 256–263.
- [13] G. Palmisano, E. Garcia-Lopez, G. Marci, V. Loddo, S. Yurdakal, V. Augugliaro, L. Palmisano, *Chemical Communications* 46 (2010) 7074–7089.
- [14] X. Chen, J. Zhang, X. Fu, M. Antonietti, X. Wang, *Journal of the American Chemical Society* 131 (2009) 11658–11659.
- [15] M. Zhang, C. Chen, W. Ma, J. Zhao, *Angewandte Chemie International Edition* 47 (2008) 9730–9733.
- [16] Y. Shiraishi, N. Saito, T. Hirai, *Journal of the American Chemical Society* 127 (2005) 12820–12822.
- [17] Y. Tominaga, T. Kubo, K. Hosoya, *Catalysis Communications* 12 (2011) 785–789.
- [18] K. Inumaru, M. Murashima, T. Kasahara, S. Yamanaka, *Applied Catalysis B* 52 (2004) 275–280.
- [19] S. Ghosh-Mukerji, H. Haick, M. Schwartzman, Y. Paz, *Journal of the American Chemical Society* 123 (2001) 10776–10777.
- [20] X. Shen, L. Zhu, J. Li, H. Tang, *Chemical Communications* (2007) 1163–1165.
- [21] X. Shen, L. Zhu, H. Yu, H. Tang, S. Liu, W. Li, *New Journal of Chemistry* 33 (2009) 1673–1679.
- [22] X. Shen, L. Zhu, G. Liu, H. Yu, H. Tang, *Environmental Science and Technology* 42 (2008) 1687–1692.
- [23] J.C. Colmenares, M.A. Aramendia, A. Marinas, J.M. Marinas, F.J. Urbano, *Applied Catalysis A: General* 306 (2006) 120–127.
- [24] H. Kominami, T. Nakaseko, Y. Shimada, A. Furusho, H. Inoue, S.-y. Murakami, Y. Kera, B. Ohtani, *Chemical Communications* (2005) 2933–2935.
- [25] J. Lee, H. Park, W. Choi, *Environmental Science and Technology* 36 (2002) 5462–5468.
- [26] Y. Kuwahara, H. Yamashita, *Journal of Materials Chemistry* 21 (2011) 2407–2416.
- [27] S. Ikeda, H. Kobayashi, Y. Ikoma, T. Harada, T. Torimoto, B. Ohtani, M. Matsumura, *Physical Chemistry Chemical Physics* 9 (2007) 6319–6326.
- [28] S. Ikeda, Y. Ikoma, H. Kobayashi, T. Harada, T. Torimoto, B. Ohtani, M. Matsumura, *Chemical Communications* (2007) 3753–3755.
- [29] S. Zhan, D. Chen, X. Jiao, Y. Song, *Chemical Communications* (2007) 2043–2045.
- [30] F.X. Llabrés i Xamena, P. Calza, C. Lamberti, C. Prestipino, A. Damin, S. Bordiga, E. Pelizzetti, A. Zecchina, *Journal of the American Chemical Society* 125 (2003) 2264–2271.
- [31] Y. Shiraishi, D. Tsukamoto, T. Hirai, *Langmuir* 24 (2008) 12658–12663.
- [32] G. Zhang, W. Choi, S.H. Kim, S.B. Hong, *Journal of Hazardous Materials* 188 (2011) 198–205.
- [33] R. Ma, T. Sasaki, *Advanced Materials* 22 (2010) 5082–5104.
- [34] Y. Ide, Y. Nakasato, M. Ogawa, *Journal of the American Chemical Society* 132 (2010) 3601–3604.
- [35] A. Takagaki, C. Tagusagawa, S. Hayashi, M. Hara, K. Domen, *Energy & Environmental Science* 3 (2010) 82–93.
- [36] Q. Xiang, J. Yu, M. Jaroniec, *Chemical Communications* 47 (2011) 4532–4534.
- [37] S. Liu, J. Yu, M. Jaroniec, *Journal of the American Chemical Society* 132 (2010) 11914–11916.
- [38] S. Liang, L. Wu, J. Bi, W. Wang, J. Gao, Z. Li, X. Fu, *Chemical Communications* 46 (2010) 1446–1448.
- [39] Y. Hosogi, K. Tanabe, H. Kato, H. Kobayashi, A. Kudo, *Chemistry Letters* 33 (2004) 28–29.
- [40] Y. Hosogi, Y. Shimodaira, H. Kato, H. Kobayashi, A. Kudo, *Chemistry of Materials* 20 (2008) 1299–1307.
- [41] X. Chen, X. Wang, Y. Hou, J. Huang, L. Wu, X. Fu, *Journal of Catalysis* 255 (2008) 59–67.
- [42] J.D. Donaldson, W. Moser, W.B. Simpson, *Journal of the Chemical Society* (1963) 1727–1731.
- [43] S. Liang, X. Wang, Y. Chen, J. Zhu, Y. Zhang, X. Wang, Z. Li, L. Wu, *Nanoscale* 2 (2010) 2262–2268.
- [44] J. Zhao, T. Wu, K. Wu, K. Oikawa, H. Hidaka, N. Serpone, *Environmental Science and Technology* 32 (1998) 2394–2400.
- [45] T. Watanabe, T. Takizawa, K. Honda, *Journal of Physical Chemistry* 81 (1977) 1845–1851.
- [46] S. Liang, S. Zhu, Y. Chen, W. Wu, X. Wang, L. Wu, *Journal of Materials Chemistry* 22 (2012) 2670–2678.
- [47] Y. Yan, M. Zhang, K. Gong, L. Su, Z. Guo, L. Mao, *Chemistry of Materials* 17 (2005) 3457–3463.
- [48] A.C. Pradhan, K.M. Parida, B. Nanda, *Dalton Transactions* 40 (2011) 7348–7356.
- [49] S. Ge, L. Zhang, *Environmental Science and Technology* 45 (2011) 3027–3033.